Integration of Earth-based materials in 3D concrete printing (3DCP): Physico-chemical and Technological characterization.

Fatima-Zahra Oulkhir[1]*, *Nadir* Rihani[1], *Iatimad* Akhrif[1], and *Mostapha* El Jai[1,2]

[1] Euromed University of Fes, Fes, Morocco
[2] ENSAM-Meknes, Moulay Ismail University, Meknes, Morocco

Abstract. The overall goal of this study is to support the advancement of new construction methods and materials that are more cost-effective and have lower carbon emissions. There is a rising interest in utilizing earth materials in 3DCP for sustainable construction solutions, but their progress is limited by slow production rates. This research investigated the influence of various parameters on the efficacy of 3D earth materials printing using Taguchi experimental design, such as alginate dosing, scan strategy, scan speed, layer thickness, and curing age. Moreover, the impact of incorporating 2% alginate biopolymer into the clay matrix was assessed through FT-IR and XRD analysis. Additionally, the Taguchi method was assessed using Fault Tree Analysis FTA to pinpoint the primary causes of failure in extrudability and buildability functions.

Keywords. 3DCP, earth materials, alginate, failure mode, fault tree analysis

1. Introduction

The construction industry is recognized as a sector that demands a wide range of resources and is associated with significant environmental challenges. Buildings alone account for 36% of total energy consumption, 40% of solid waste production, 12% of potable water usage, and 38% of greenhouse gas emissions, as well as 8% of global anthropogenic CO_2 emissions [1], [2]. Moreover, the industry has been criticized for its subpar productivity levels [3], [4]. To address these issues, Additive manufacturing (AM) or 3D-printing technology has been introduced to the construction industry, aiming to deliver rapid, dependable, and cost-efficient construction solutions, while enabling the creation of intricate designs with enhanced aesthetics. This innovative technology has been proven to lower construction expenses, boost productivity, and offer additional advantages such as decreased carbon emissions and waste, design flexibility, and enhanced accuracy [5]–[9]. The initial stages of 3D concrete printing (3DCP) involve creating a digital model, selecting the appropriate materials, and setting up the printer. Essentially, this approach relies on a computer-controlled system to produce the model that will be printed [10], [11]. In addition, since 3DCP is considered as one of the

* Corresponding author: f.oulkhir@ueuromed.org

latest cutting edge technologies in AM in the 21st century, it is then noteworthy that it has beneficiated of all the advanced that were developed in AM realm in terms of extrusion control technologies [12]–[14], topology optimization [15], generative design [7], [8], scanning strategies optimization [16], [17], and other specific tools such as image processing and data analysis applied to AM [18]–[20].

Conversely, a wide range of materials utilized in 3DCP, such as cementitious materials, alkali-activated materials known as geopolymers, and hybrid materials where geopolymers partially replace cement, are being explored in light of environmental concerns associated with Portland cement materials [21]. The need for alternatives that are more energy-efficient and environmentally friendly is becoming increasingly urgent.

In this regard, the use of 3DCP based on earth materials is a emerging method for the production of low-carbon structures [22], [23]. However, the progress of earthen construction is still limited by insurance challenges and poor durability caused by high susceptibility to water [23], [24]. Efforts have been made to address the instability, and mechanical problems of earth binders by considering the inclusion of stabilizing additives. These additives consist of fibers, mineral additives, and biopolymers [23]–[26].

Furthermore, the efficacy of 3DCP is contingent upon the success of each phase of the 3DCP process, which includes pumpability, extrudability, and buildability [21], [27]. This necessitates the adjustment of parameters that impact the success of 3DCP, such as mix-design parameters and printing parameters [28], [29]. Hence, this research paper focuses on investigating the influence of variable parameters on both undoped and doped marl behavior using a Taguchi experimental design on the success of extrudability, and buildability stages. These parameters include the integration of alginate biopolymer within the marl matrix, scan speed, scan strategy, layer thickness, and curing age. The assessment of the system under study is conducted through the utilization of a quality management tool, Fault Tree Analysis (FTA), to pinpoint the root causes of 3DCP failures.

The subsequent sections of the paper are structured as follows: Section 2, Materials and Methods, outlines the characterization and physicochemical properties of the raw materials, the synthesis process undertaken, and the methodologies employed to evaluate the performance of 3D-printed composites, including FT-IR spectroscopy, XRD analysis to evaluate the effect of alginate addition on chemical and structural properties, 3D-printing tests, and Fault Tree Analyses FTA. Conversely, Section 3 presents the findings derived from the printed and cast composites. Lastly, Section 4 provides the concluding remarks and highlights potential avenues for future

2. Materials and methods

2.1. Raw materials

The raw marl was gathered from the eastern lower part of the Sais basin at the Benjallik quarry with coordinates: longitude 4°56'56.9" W, latitude 34°02'14.8" N, and an altitude of 431m. To prepare the clayey soil for this research, the rocky clay was crushed into small pieces using a mortar and then dried at 100 °C to eliminate moisture. Subsequently, a Retsch RM200 grinder was used to refine the clay particles. The raw clay was then sieved, with particles of 212 µm selected for the study. The physical and chemical properties of the raw marl from the Fez region are detailed in tables 1 and 2.

Sodium alginate, a biopolymer derived from brown algae, consists of two repeating units: β-1,4-linked D-mannuronic acid (M block) and α-1,4-linked guluronic acid (G block) [30],

[31]. It was acquired by ERBApharm to study its effects on the printability of the samples that were prepared.

Table 1. Physicochemical parameters of raw marl

Physicochemical parameters	**Values**
Plastic limit (%)	26.97
Liquid limit (%)	43.38
Plasticity index (%)	16.42
Water content (w%)	45.5
Bulk density (g/cm^3)	2.19
Specific surface area S_{BET} (m^2/g)	28.31

Table 2. The chemical composition of Fez clay [32], [33]

SiO_2	Al_2O_3	F_2O_3	CaO	MgO	Cr_2O_3	K_2O	Na_2O	Ti_2O	MnO_2
44.9%	15.1%	6.49%	6.64%	3.08%	1.84%	1.10%	0.80%	0.37%	0.20%

2.2. Preparation method

The study employed a Taguchi experimental design, incorporating 5 selected parameters: layer thickness, alginate content, scan strategy, scan speed, and water age. The experimental design used is detailed in tables 3, and 4. The synthesis process began with mixing solid precursors (marl and sodium alginate) for 5 minutes, followed by the addition of water and an additional 5 minutes of mixing. The experimental procedure is illustrated in Fig.1.

The fresh mixture was deposited layer by layer using a 3D Potter 10 Pro printer robot controlled by a G-code generated by Simplify software. The nozzle had a circular cross-section of 5 mm. To assess the impact of the 5 Taguchi parameters, 18 cubic specimens measuring 40 nm×40 mm×40 mm were prepared. Additionally, casted samples were made in a cubic cast with the same dimensions to investigate the effect of alginate content further. Finally, the printed and cast specimens were cured at ambient temperature.

Table 3. Prepared mixture proportions

Mixtures	**Clay (g)**	**Alginate (g)**	**Alginate (%)**	**Water (g)**	**Water (%)**
undoped marl	300	-	-	112.5	27.27%
Doped marl	300	6.12	2%	200	40%

Table 4. Prepared mixture proportions

Combination	Alg (%)	Scan strategy	Scan speed (mm/min)	Layer thickness (mm)	Age (days)
TAG 1	0	45;-45	500	1.4	7
TAG 2	0	45;-45	500	1.4	14
TAG 3	0	45;-45	500	1.4	21
TAG 4	0	0;90	650	2	7
TAG 5	0	0;90	650	2	14
TAG 6	0	0;90	650	2	21
TAG 7	0	-45;0;45;90	800	2.6	7
TAG 8	0	-45;0;45;90	800	2.6	14
TAG 9	0	-45;0;45;90	800	2.6	21
TAG 10	2	45;-45	650	2.6	7
TAG 11	2	45;-45	650	2.6	14
TAG 12	2	45;-45	650	2.6	21
TAG 13	2	0;90	800	1.4	7
TAG 14	2	0;90	800	1.4	14
TAG 15	2	0;90	800	1.4	21
TAG 16	2	-45;0;45;90	500	2	7
TAG 17	2	-45;0;45;90	500	2	14
TAG 18	2	-45;0;45;90	500	2	21

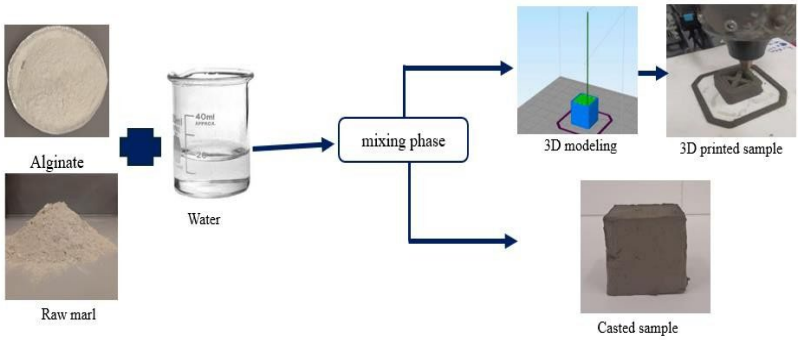

Fig. 1. Experimental procedure of prepared mixtures

2.3. Characterization

The FT-IR analysis was conducted using the Alpha II, Brucker spectrometer to investigate the chemical structure of sodium alginate, raw marl, and alginate-marl composite within the wavelength range of 400-4000 cm^{-1}, with a resolution of 4 cm^{-1}. Additionally, the XRD anal-

ysis was performed using the Brucker D8 advanced X-ray diffractometer to study the mineralogical composition and crystalline structure of raw precursors and doped marl, operating at 40 kV and using Cu-Kα monochromatic radiation (λ = 1.5418 Å). The printability test was used to assess each combination's extrudability and buildability properties. At the same time, the behavior of prepared samples after 14 days of curing was evaluated to determine the impact of mix design and printing parameters on mixture stability. Finally, a Fault Tree Analysis FTA was conducted to identify the main causes of 3D printing failure in the prepared samples.

3. Results and discussion

3.1. FT-IR spectroscopy

The FT-IR spectra of sodium alginate, undoped marl, and 2% doped marl are shown in Fig. 2. In the FT-IR pattern of alginate, a broad peak ranging from 3062-3468 cm^{-1} is observed, corresponding to the stretching vibration of hydroxyl groups in acids, alcohols, and adsorbed water. Peaks at 1599, 1406, and 1301 cm^{-1} are attributed to the stretching vibrations of carboxylate salt ions (COO^-), while the peak at 1028 cm^{-1} is linked to oxygen stretching in cyclic ether bridge (COC). Furthermore, stretching vibrations of aliphatic groups (CH) can be seen at 2904 cm^{-1} [34], [35].

The band observed at 3391 cm^{-1} in undoped marl indicates the stretching vibrations of (OH) groups associated with adsorbed water. Peaks at 3625 and 3701 cm^{-1} are attributed to the vibrations of inner and outer surface OH groups of Al-OH and Si-OH. Additionally, the bands at 1001cm^{-1} represent the asymmetric stretching vibrations of Si-O bonds. Conversely, the bands at 414, 465, 519, 792, and 874 cm^{-1} are associated with the bending vibrations of Si-O-Si, Si-O-Mg, Si-O-Al, Mg-Al-OH, and Fe-Al-OH bonds [36], [37], respectively. Furthermore, the presence of carbonates is assigned by the bands at 1414, and 710 cm^{-1}, which correspond to the stretching, and in-plane bending vibrations [38]. Conversely, as shown in Fig.3, it is evident that the diagnostic peaks of marl were mostly unchanged by the doping process, with slight shift of 2 cm^{-1} in certain bands, indicating the presence of weak physical interactions between alginate and the marl surface. Moreover, the absorption bands related to the biopolymer were not detected, due to the low concentration of sodium alginate.

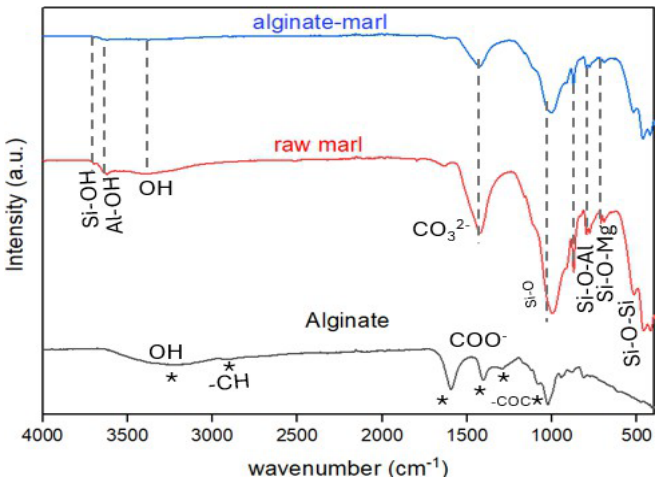

Fig. 2. FTIR-spectra of alginate, raw marl, and the alginate-doped marl

3.2. XRD analysis

The x-ray diffractogram of alginate, undoped marl, and doped marl is presented in Fig.3. The diffraction pattern of alginate displays a semi-crystalline structure with two broad diffraction peaks at 13.47° and 26.57° [39], [40]. In contrast, the raw marl exhibits distinct sharp peaks indicating its crystallinity, with the diffractogram showing the presence of non-clay minerals such as quartz and calcite and clay minerals like kaolinite, illite, and chlorite [41]–[43]. All peaks match the pattern JCPDS card NO. 005-0686 for raw marl. Based on Fig. 3, the doped marl with 2% alginate shows a similar pattern to undoped marl, with a slight shift 2θ =1° towards lower angles.

In summary, the slight shift observed in the FT-IR and XRD analysis can be explained by the weak physical interactions, including hydrogen bonds, Van der Waals interactions, and electrostatic interactions of alginate functions with the divalent cations present in the earth material, leading to the formation of a network (gel) through a process called ionic crosslinking (Fig.4) [23], [44].

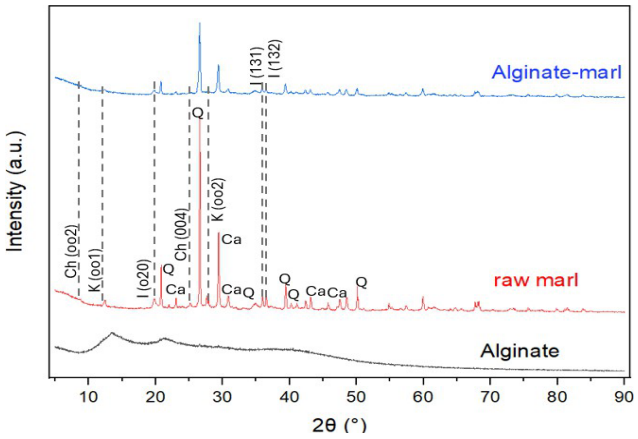

Fig. 3. XRD patterns of alginate, raw marl, and the alginate-doped marl, with **K**: Kaolinite, I: Illite, **Ch**: Chlorite, **Q**: quartz, and **Ca**: Calcite

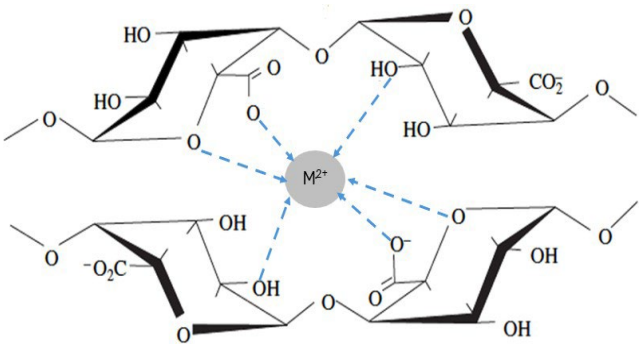

Fig. 4. Crosslinking process of alginate with cations M^{2+} from clay [44]

3.3. 3D-printing test

Fig.5 illustrates the results of the 18 combinations. 3DCP printing can be categorized into two primary service functions: printability and buildability, with printability being a combination of pumpability and extrudability [21], [29], [45]. However, this study focused on evaluating the effectiveness of extrudability and buildability. As shown in Fig.5, the 18 printed samples exhibit smooth extrusion without any blockages in the nozzle opening, segregation, or discontinuity.

Moreover, the samples without alginate biopolymer TAG1 to TAG9 showed no cold joints and strong adhesion between adjacent layers. It is also clear that the success of the buildability function is directly influenced by printing parameters such as scan strategy, scan speed, and layer thickness. The combinations TAG 7, 8, and 9 with a scan strategy of (-45;0;45;90), a scan speed of 800 mm/min, and a layer thickness of 2.6 mm exhibited flawless layer deposition and no layer tearing. On the other hand, reducing the scan speed from 800 to 500 mm/min for TAG1 to TAG6 resulted in increased tearing of the layers, and decreasing the layer thickness led to improper deposition between layers, possibly due to the pressure exerted by the printer head during printing.

The addition of 2% alginate leads to the formation of joints between layers from the first day of printing, The inadequate bonding and cold joints between layers can be attributed to alginate's ability to absorb water through hydrogen bonds, which decreases the presence of free water in the surface of printed layers, thus affecting adhesion and leading to splitting between layers. Moreover, the different combinations also demonstrate a compaction in the lower layer as a result of the plasticity behavior of the mixtures, resulting in the bottom layer being unable to support the weight of the upper layers.

Fig. 5. Evaluation of *3D-printing* of the prepared mixtures

3.4. Curing and early age behavior

The drying phase in the production of earth-based materials is critical in determining the construction pace. Throughout this phase, the microstructure consolidation and mechanical properties develop gradually. However, it is crucial to address challenges such as shrinkage, cracks, and heterogeneities, as they can have a detrimental effect on the final structure [46]. The failure modes depicted in Fig.6 were observed in both cast and printed samples. As mentioned in section 3.3, the mixture without alginate did not exhibit any failure mode in either casting or 3D printing after 14 days of curing at room temperature. However, the composite

with 2% alginate-marl showed various failure modes closely related to the mix-design and printing parameters. According to Fig.6, the failure planes could be categorized into three modes:

- The first mode involves a sample undergoing horizontal failure on the first day of printing, followed by a vertical crack, and then cracks in different directions isotopically. This mode was specifically observed in TAG10, 11, 12, 15, 16, and casted samples.
- The second mode is characterized by a cube with a vertical rupture, which was observed in TAG13, 17, and 18.
- The third mode consists of horizontal rupture, observed in TAG 14. Fig.7 provides a schematic illustration of these three modes.

The different failure modes presented demonstrate the prepared materials' heterogeneity behavior, suggesting that adding 2% alginate reduces the cohesion among clay particles due to significant water absorption. As a result, there is uneven volume change during drying, leading to the formation of cracks.

Combinations	1st-day	After 14-day of curing
Casted 0% alginate-marl		
Casted 2% alginate-marl		
TAG 10		
TAG 11		

		
TAG 12		
TAG 13		
TAG 14		
TAG 15		
TAG 16		
TAG 17		
TAG 18		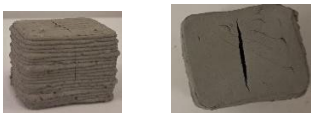

Fig. 6. Initial and final state of prepared samples after 14 days of curing at ambient temperature

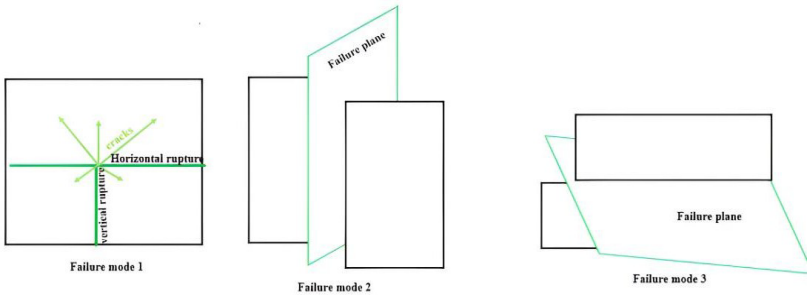

Fig. 7. Different failure modes observed on 2% alginate-marl combinations

3.5. Fault Tree Analysis (FTA)

An FTA is a technique used to pinpoint an unfavorable condition within a system by utilizing logical combinations [47]. The 3DCP fault trees were specifically designed to identify the fundamental and intermediate events that lead to undesired intermediate events such as fault printability and fault buildability, which ultimately impact the occurrence of the main event (fault 3DCP) [21]. In this research, FTA is utilized to recognize all undesirable events during the extrudability and buildability phases, for both doped and undoped marl. Fig.8 illustrates the FTA analysis conducted in this research. Consequently, Table 5 translates the logical relationships among the events shown in Fig.8 into logical equations. The exclusive use of "OR" gates in this study indicates that the Fault 3DCP top undesired event and other undesired events can be dissected into sub-events for further analysis.

The top event, Fault 3DCP ($\overline{UE}$) is influenced by two intermediary events: either Fault Extrudability ($\overline{TF1.2}$) OR Fault Buildability ($\overline{SF2}$).

- **Fault Extrudability** ($\overline{TF1.2}$) is a result of two sub-intermediate events: tearing of layers (event A) and Uninterrupted material extrusion (event B). The tearing of layers can be caused by inappropriate scan speed (event 1), the presence of voids (event A1) due to air bubbles present in the materials during the filling process, the scan strategy chosen (event 3), or the high stiffness of mixtures (event A2) caused by the addition of alginate (event 4). On the other hand, Uninterrupted material extrusion occurs due to the retraction effect during the printing process (event 5) when the nozzle does not stop material extrusion before moving.
- **Fault Buildability** is the result of four sub-intermediary events. These events include the compaction of bottom layers (event C), which is caused by low layer thickness (event 6), or it can be influenced by the weak consistency of mixtures (event C1), which in turn can be attributed to the addition of alginate and water ratio (event 7). The mal interlayer deposition (event D) is specifically caused by low layer thickness, while the weak adhesion of layers (event E) is related to the alginate content. Additionally, the presence of cracks (event F) is due to both the alginate content and scan strategy.

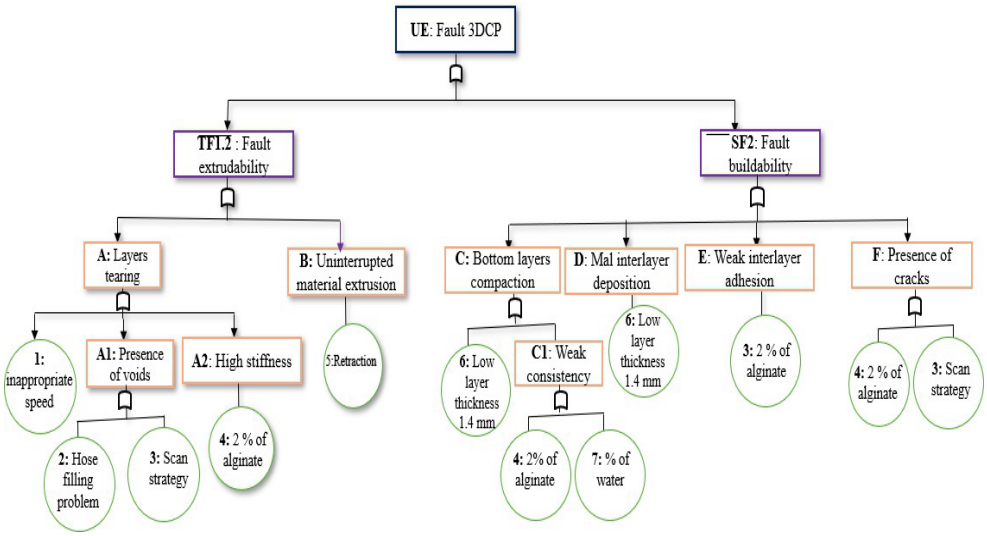

Fig. 10. Fault Tree Analysis FTA of the study

Table 5. FTA Boolean equations for this study

$UE = \overline{TF1.2} + \overline{SF2}$	
$\overline{TF1.2}$ = A + B	$\overline{SF2}$ = C + D + E + F
A = A1 + A2 + 1	C = C1 + 6
A1 = 2 + 3	C1 = 4 + 7
A2 = 4	D = 6
B = 5	E – 3
	F = 4 + 3
	G = 5

4. Conclusion

This research has demonstrated the potential of utilizing Fez-Taza marl as a binding agent in 3DCP, and the challenges associated with both undoped and doped marl in achieving high productivity. The study focused on exploring physicochemical interactions, 3D printabil- ity, and various failure modes associated to 0% and 2% alginate-marl mixtures. The conclusions drawn from the results are as follows:

- The slight shift in both FR-IR and XRD patterns is attributed to the ionic crosslinking (gelling process) between the alginate functional groups and clay cations through physical interactions such as hydrogen bonds, electrostatic, and Van Der Waals interactions.

- The 3D-printing test highlighted the impact of mixture parameters (alginate content, scan strategy, scan speed, layer thickness, and age) on the extrudability and buildability functions. It was observed that samples with 2% alginate TAG 10 to TAG 18 exhibited a failure in buildability function, leading to a failure in the 3DCP system.

- After 14 days of curing, both cast and printed samples displayed different ruptures, particularly for the doped marl, which subsequently affected their mechanical properties. These ruptures were categorized into three modes based on the failure plan. The first mode involved horizontal failure on the first day of printing, followed by a vertical crack and then cracks in different directions. The second mode was characterized by vertical failure and the third mode by horizontal failure.

- The FTA analysis outlined the intermediate events and basic events contributing to the top event 3DCP faults. According to this analysis, the most observed failures were: extrudability faults, layers tearing and uninterrupted material extrusion, and buildability faults, bottom layers compaction, mal layers deposition, weak interlayer adhesion, and the presence of cracks.

This study on the feasibility of earth 3D printing provides a solid foundation for further investigations into optimizing mixture parameters using earth materials in 3DCP, and understanding their effects on the properties of 3D printed earth materials during the fresh and hardening stages.

Reference:

[1] M. K. Mohan, A. V. Rahul, G. De Schutter, and K. Van Tittelboom, Extrusion-based concrete 3D printing from a material perspective: A state-of-the-art review. *Cem. Concr. Compos*. **115**, 103855 (2021). https://doi.org/10.1016/j.cemconcomp.2020.103855.

[2] Y. A. Al-Noaimat, S. H. Ghaffar, M. Chougan, and M. J. Al-Kheetan, A review of 3D printing low-carbon concrete with one-part geopolymer: Engineering, environmental and economic feasibility. *Case Stud. Constr. Mater.***18**, e01818 (2023). https://doi.org/10.1016/j.cscm.2022.e01818.

[3] P. Wu, J. Wang, and X. Wang, A critical review of the use of 3-D printing in the construction industry. *Autom. Constr.* **68**, 21–31(2016). https://doi.org/10.1016/j.autcon.2016.04.005.

[4] G. L. F. Benachio, M. do C. D. Freitas, and S. F. Tavares, Circular economy in the construction industry: A systematic literature review. *J. Clean. Prod.* **260**, 121046, (2020). https://doi.org/10.1016/j.jclepro.2020.121046.

[5] K. Gamage, S. Fawzia, T. Zahra, M. B. F. Teixeira, and N. H. Ramli Sulong, Advancement in Sustainable 3D Concrete Printing: A Review on Materials, Challenges, and Current Progress in Australia. *Buildings*, **14**, (2024). https://doi.org/10.3390/buildings14020494.

[6] S. Inayath Basha, A. Ur Rehman, H. R. Khalid, M. A. Aziz, and J. H. Kim, 3D Printable Geopolymer Composites Reinforced with Carbon-Based Nanomaterials – A Review. *Chem. Rec.* **10**. 202300054 (2023). https://doi.org/10.1002/tcr.202300054.

[7] N. Rihani, I. Akhrif, M. El Jai, and L. Mohamed, Finite Element modeling and convergence analysis of a new Biomimetic Branching Structures. *Stat. Optim. Inf. Comput.***12**, 713–726 (2024). https://doi.org/10.19139/SOIC-2310-5070-1964.

[8] N. Rihani, I. Akhrif, and M. El Jai, Proposition and design of a new Micro-Architected Domes family: A biomimicry-based approach. *Front. Archit. Res.* **13**, 650–667 (2024). https://doi.org/10.1016/j.foar.2024.01.004.

[9] K. El Abbaoui, I. Al Korachi, M. El Jai, B. Šeta, and M. T. Mollah, 3D concrete printing using computational fluid dynamics: Modeling of material extrusion with slip boundaries. *J. Manuf. Process.***118**, 448–459 (2024). https://doi.org/10.1016/j.jmapro.2024.03.042.

[10] M. Dadkhah, J. M. Tulliani, A. Saboori, and L. Iuliano, Additive manufacturing of ceramics: Advances, challenges, and outlook. *J. Eur. Ceram. Soc.* **43**, 6635–6664 (2023). https://doi.org/10.1016/j.jeurceramsoc.2023.07.033.

[11] N. Youssef, A. Z. Rabenantoandro, Z. Lafhaj, Z. Dakhli, F. Hage Chehade, and L. Ducoulombier, A novel approach of geopolymer formulation based on clay for additive manufacturing. *Constr. Robot.* **5**, 175–190 (2021). https://doi.org/10.1007/s41693-021-00060-1.

[12] K. Ouazzani, I. Akhrif, N. Rihani, M. El Jai, M. Radouani, and B. El Fahime, Processing Parameters, Heat-Treatment, and Testing Speed influence on Tensile properties of ABS-FDM materials. *Moroccan J. Chem.* **12**, 1621–1663 (2024).

https://doi.org/10.48317/IMIST.PRSM/morjchem-v12i4.50175.

[13] K. Ouazzani, M. El Jai, I. Akhrif, M. Radouani, and B. El Fahime, An experimental study of FDM parameter effects on ABS surface quality: roughness analysis. *Int. J. Adv. Manuf. Technol.* **127**, 151–178 (2023). https://doi.org/ 10.1007/s00170-023-11435-9.

[14] K. Ouazzani, M. El Jai, and B. Elfahime, Detailed classification of FDM (Fused Deposition Modeling) process parameters and potentially affected Part characteristics. *2022 2nd Int. Conf. Innov. Res. Appl. Sci. Eng. Technol. IRASET 2022*, (2022). https://doi.org/10.1109/IRASET52964.2022.9738432.

[15] M. El Jai, N. Saidou, M. Zineddine, and H. Bachiri, Mathematical design and preliminary mechanical analysis of the new lattice structure: 'GE-SEZ*' structure processed by ABS polymer and FDM technology. *Prog. Addit. Manuf.* **6**, 93–118 (2021). https://doi.org/10.1007/s40964-020-00148-0.

[16] M. El Jai, I. Akhrif, and N. Saidou, Skeleton-based perpendicularly scanning: a new scanning strategy for additive manufacturing, modeling and optimization. *Prog. Addit. Manuf.* **6**, 781–820 (2021). https://doi.org/10.1007/s40964-021-00197-z.

[17] M. El Jai and I. Akhrif, SBPar scanning : Toward a complete optimal skeleton scan strategy for Additive Manufacturing. (2024).

[18] N-C. Igwe, I. Akhrif, and M. El Jai, An experimental investigation of the influence of SLM input factors on the as-built AlSi10Mg surface quality. *Int. J. Adv. manuufacturing Technol.* (2024). https://doi.org/10.1007/s00170-024-14657-7.

[19] K. Fri, A. Laazizi, M. Bensadaa, M. El Alami, A. Ouannou, I. Akhrif, M. El Jai, and J,Fajoui, Microstructural and heat treatment analysis of 316L elaborated by SLM additive manufacturing process. *Int. J. Adv. Manuf. Technol.* **124**, 2289–2297, (2023). https://doi.org/10.1007/s00170-022-10622-4.

[20] K. Fri, I. Akhrif, A. Laazizi, M. El Jai, M. Bensada, and A. Ouannou, Experimental investigation of the effects of processing parameters and heat treatment on SS 316L manufactured by laser powder bed fusion. *Prog. Addit. Manuf.* (2023). https://doi.org 10.1007/s40964-023-00538-0.

[21] F. Z. Oulkhir, I. Akhrif, and M. El Jai, *3D concrete printing success: an exhaustive diagnosis and failure modes analysis*. *Prog. Addit. Manuf.* (2024). https://doi.org/10.1007/s40964-024-00638-5.

[22] A. Curth, N. Pearl, A. Castro-Salazar, C. Mueller, and L. Sass, 3D printing earth: Local, circular material processing, fabrication methods, and Life Cycle Assessment. *Constr. Build. Mater.*, **421**, 135714 (2024). https://doi.org/10.1016/j.conbuildmat.2024.135714.

[23] Y. Maierdan, M. Samuel J, Armistead Rebecca A, Q. Huang, B.-A. Lola, S. I. Wil V, and K. Shiho, Rheology and 3D printing of alginate bio-stabilized earth concrete. *Cem. Concr. Res.* **175**, 107380 (2024). https://doi.org/10.1016/j.cemconres.2023.107380.

[24] A. Perrot, D. Rangeard, and E. Courteille, 3D printing of earth-based materials: Processing aspects. *Constr. Build. Mater.* **172**, 670–676 (2018). https://doi.org/10.1016/j.conbuildmat.2018.04.017.

[25] F. Faleschini, D. Trento, M. Masoomi, C. Pellegrino, and M. A. Zanini, Sustainable mixes for 3D printing of earth-based constructions. *Constr. Build. Mater.*, **398**, 132496 (2023). https://doi.org/10.1016/j.conbuildmat.2023.132496.

[26] S. Rückrich, G. Agranati, and Y. J. Grobman, Earth-based additive manufacturing: A field-oriented methodology for evaluating material printability. *Archit. Sci. Rev.* **66**, 133–143 (2023). https://doi.org/10.1080/00038628.2022.2154739.

[27] A. Paolini, S. Kollmannsberger, and E. Rank, Additive manufacturing in construction : A review on processes , applications , and digital planning methods. *Addit. Manuf.* **30**, (2019). https://doi.org/10.1016/j.addma.2019.100894.

[28] A. U. Rehman, Jung-Hoon, and Kim, 3D concrete printing: A systematic review of rheology, mix designs, mechanical, microstructural, and durability characteristics. *Materials (Basel).***14**, 1–43 (2021, https://doi.org/10.3390/ma14143800.

[29] S. C. Paul, Y. W. D. Tay, B. Panda, and M. J. Tan, Fresh and hardened properties of 3D printable cementitious materials for building and construction. *Arch. Civ. Mech. Eng.* **18**, 311–319 (2018). https://doi.org/10.1016/j.acme.2017.02.008.

[30] M. Abdollahi, M. Alboofetileh, M. Rezaei, and R. Behrooz, Comparing physico-mechanical and thermal properties of alginate nanocomposite films reinforced with organic and/or inorganic nanofillers. *Food Hydrocoll.* **32**, 416–424 (2013). https://doi.org/10.1016/j.foodhyd.2013.02.006.

[31] N. D. B. Mignon, Arn, Didier Snoeck, Kenny D'Halluin, Lieve Balcaen, Frank Vanhaecke, Peter Dubruel, Sandra Van Vlierberghe, Alginate biopolymers: Counteracting the impact of superabsorbent polymers on mortar strength. *Constr. Build. Mater.***110**, 169–174 (2016). https://doi.org/10.1016/j.conbuildmat.2016.02.033.

[32] M. El Halim, L. Daoudi, M. El Ouahabi, and N. Fagel, Characterization of clays from the Fez area (northern Morocco) for potential uses in the ceramics industry. *Clay Miner.* **57**,139–149 (2022). https://doi.org/10.1180/clm.2022.30.

[33] L. Mesrar, I. Akhrif, and R. Jabrane, Technological Characterization of the Miocene Marl in the Region of Taza (Morocco): Exploitation Possibilities. *Int. J. Res. Sci.* **2**, 8–13 (2014).

[34] L. Qin, C. Guo, Q. Guo, H. Yi, and F. Jia, 3D montmorillonite aerogel/SA composite phase change materials with mechanically strong strength and superior thermal energy storage performances. *Miner. Miner. Mater.* **2**, (2023). https://doi.org/10.20517/mmm.2023.20.

[35] R. Surya, M. D. Mullassery, N. B. Fernandez, and D. Thomas, Synthesis and characterization of a clay-alginate nanocomposite for the controlled release of 5-Flurouracil, *J. Sci. Adv. Mater. Devices*, **4**, 432–441 (2019). https://doi.org/ 10.1016/j.jsamd.2019.08.001.

[36] S. Ghyati, S. Kassou, M. El Jai, E. H. El Kinani, and M. Benhamou, Investigation of PEG4000/Natural clay-based hybrids: Elaboration, characterization and theory. *Mater. Chem. Phys.* **239**, (2020). https://doi.org/10.1016/j.matchemphys.2019.121993.

[37] A. Maged, S. A. Abu El-Magd, A. E. Radwan, S. Kharbish, and S. Zamzam,

Evaluation insight into Abu Zenima clay deposits as a prospective raw material source for ceramics industry: Remote Sensing and Characterization. *Sci. Rep.***13**, 1–16, (2023). https://doi.org/10.1038/s41598-022-26484-5.

[38] S. Hajji, T. Turki, A. Boubakri, M. Ben Amor, and N. Mzoughi, Study of cadmium adsorption onto calcite using full factorial experiment design. *Desalin. Water Treat.* **83**, 222–233 (2017). https://doi.org/10.5004/dwt.2017.21079.

[39] S. Bhagyaraj and I. Krupa, Alginate-mediated synthesis of hetero-shaped silver nanoparticles and their hydrogen peroxide sensing ability. *Molecules*, **25**, (2020), https://doi.org/10.3390/molecules25030435.

[40] F. Sentanin, C. Caliman, WR. Sabadini, RC. Cavalheiro, R. Pereira, M. Silva, and A. Pawlicka, Nanocomposite polymer electrolytes of sodium alginate and montmorillonite clay. *Molecules*, **26**, 1–11 (2021). https://doi.org/10.3390/molecules26082139.

[41] B. Achiou, H. El Omari, J. Bennazha, A. Albizane, L. Daoudi, L.Saadi, M. Ouammou, SA. Younssi, A. El Maadi, Physicochemical and mineralogical characterizations of clays from Fez region (basin of Saiss, Morocco) in the perspective of industrial use. *J. Mater. Environ. Sci*, **7**, 1474–1484, (2016).

[42] I. Akhrif, L. Mesrar, M. E. L. Jai, M. Benhamou, and R. Jabrane, Elaboration and X-Ray Diffraction Techniques Characterization of clay-PEG 6000 Nanocomposites with clay Matrix. **3**, 564–571 (2015).

[43] I. Akhrif, M. El Jai, L. Mesrar, A. Elkhalfi, A. Touache, and R. Jabrane, Physical Characterization and Elaboration Discussion of a Clay-PEG 6000 Composite with Natural Clay Matrix. *Engineering*, **6**, 338–354 (2014). https://doi.org/10.4236/eng.2014.67037.

[44] J. P. Engbert, Alexander, Stefanie Gruber, The effect of alginates on the hydration of calcium aluminate cement. *Carbohydr. Polym.* **236**, (2020). https://doi.org/10.1016/j.carbpol.2020.116038.

[45] Y. Zhang, Y. Zhang, G. Liu, Y. Yang, M. Wu, and B. Pang, Fresh properties of a novel 3D printing concrete ink. *Constr. Build. Mater. 174*, 263–271 (2018). https://doi.org/10.1016/j.conbuildmat.2018.04.115.

[46] E. Keita and A. Perrot, Processing of earth-based materials: current situation and challenges ahead. *RILEM Tech. Lett*. **8**, 141–149 (2023). https://doi.org/10.21809/rilemtechlett.2023.186.

[47] S. Kabir, An overview of fault tree analysis and its application in model based dependability analysis. *Expert Syst. Appl.* **77**, 114–135 (2017), https://doi.org/10.1016/j.eswa.2017.01.058.